PIER C

(Received 15 January 2025, Accepted 19 February 2025, Scheduled 3 March 2025)

Improved Model Predictive Torque Control Strategy Incorporating Decoupled Sliding Mode Disturbance Observer for PMSM

Yang Zhang[1], Ping Yang[1], Kun Cao[1], Yang Gao[1], Gao Tang[1], and Qing Chen[2,*]

[1] *Hunan University of Technology, Zhuzhou 412007, China*
[2] *Hunan Railway Professional Technology College, Zhuzhou 412001, China*

ABSTRACT: Aiming at the problems of adjusting the weighting factor, significant torque ripple, and insufficient robustness against load disturbances in conventional model predictive torque control (MPTC) for PMSM, an improved model predictive torque control (IMPTC) strategy incorporating a decoupled sliding mode disturbance observer (DSMDO) is proposed. Firstly, the cost function is divided into two components, and both of them are evaluated sequentially to eliminate the need for weighting factors. Secondly, the set of candidate voltage vectors (VVs) is expanded by the VVs modulation technique to reduce the torque ripple, and a low-complexity method is introduced to determine the sector. Subsequently, the action time of the optimal VV is further corrected, which enhances the control of flux while reducing computational complexity. Additionally, a novel sliding mode disturbance observer with decoupling capability is introduced, which offers feedforward compensation to the speed loop and improves system robustness against disturbances. Finally, the correctness and effectiveness of the proposed IMPTC strategy with DSMDO are proved by the experimental results.

1. INTRODUCTION

Permanent magnet synchronous motors (PMSMs) are widely used in various industries, including servo drive systems, wind power generation, and railway transportation, due to their superior performance [1, 2]. The advancement of digital microprocessing technology has heightened the interest in model predictive torque control (MPTC) [3–5]. This interest is attributed to its intuitive principles, rapid response capabilities, and ability to optimize multiple objectives, variables, and constraints. In conventional MPTC, the voltage vectors are selected by evaluating a cost function. It typically includes both torque and stator flux. Given that torque and flux lie in different dimensions, establishing a suitable weighting factor is crucial for achieving optimal control [6]. In many instances, the weighting factor is determined through error handling experience and tremendous trial, which are both tedious and time-consuming. For example, [7, 8] pointed out that when there are more weighting factors and a large range of values, the worst case requires exponential simulation with extremely high computational and time overhead. In addition, the weight adjustment error is about 20%, which makes it easy to fall into local optimality and has limited generalization ability. As a result, it is not widely accepted.

Several solutions have been proposed to address the tuning of the weighting factor in MPTC [9–18]. In [9], an online adjustment strategy for the weighting factor was proposed. However, the mathematical expressions are complex and highly dependent on parameter accuracy, which significantly elevates the system's computational complexity. As introduced in [10], a genetic algorithm, informed by an artificial neural network, was proposed to determine the optimal weighting factor. However, this method still imposes a significant computational burden due to the requirement for extensive offline training. To solve this problem, a look-up table approach was employed to ascertain the best weighting factor directly [11]. Nonetheless, in unexpected load changes, the weighting factor may not be adjusted in time, leading to a decline or failure in control performance. Compared to online optimization methods, this approach has weaker adaptive capabilities. In [12], a torque-flux error plane was developed to relate the weighting factors to the voltage vectors, and evaluation criteria were used to select the best weighting factor. The derivation of this approach is more complex. In [13], the relationship between the dynamic and static properties of torque and flux was analyzed, and a method of state normalization and variable sensitivity balancing was used to adjust the weighting factor. These methods exhibit limited robustness to parameter variations, necessitating complex computations to ascertain the weighting factor.

Consequently, an increasing number of researchers are focusing on ways to eliminate the weighting factor. In [14] and [15], the cost function is redefined to include only the d-q axis stator flux chain, thus eliminating the need for weighting factor adjustment. Similarly, [16] examines the relationship between the stator flux phase angle and electromagnetic torque, leading to a simplified cost function that consists solely of the torque term. Further, in [17], it is reformulated into a voltage vector error cost function with a fast vector selection. In [18], a novel cost function that includes speed and current errors is introduced. This design eliminates the need for ad-

* Corresponding author: Qing Chen (chenqing800817@sina.com).

justing the weighting factor, and the speed and current can be optimized. Although these methods achieve satisfactory control performance without relying on a weighting factor, their underlying structures remain relatively complex and less intuitive.

A structurally straightforward MPTC strategy, sequential model predictive torque control (SMPTC), has been introduced that eliminates the need for a weighting factor [19]. This approach divides the cost function into two distinct components and utilizes a sequential structure, evaluating the torque cost function first, followed by the flux. The cascade structure adopted by SMPTC is extremely simple and intuitive, making it easy to implement. In [20], a generalized sequential model predictive control (GSMPTC) strategy is presented, enabling a flexible execution order for the two cost functions. This flexibility leads to a relative improvement in control performance. In [21], the tolerant sequential model predictive control (TSMPTC) strategy is presented. This approach sets a torque cost function tolerance based on performance requirements. Voltage vectors that meet the tolerance could be fed into the next cost function, with the number of second level vectors varying according to those that satisfy the tolerance. Compared to traditional SMPTC, although this strategy reduces torque ripple, it falls far short of being adequate in practical applications. All the aforementioned methods optimize within only eight basic voltage vectors, which limits the torque control effect. This leads to significant current fluctuations within a cycle, causing larger torque and flux ripple.

Considering that the motor will have sudden changes in load during actual operation, the dynamic performance of the motor will be affected. In [22], a control strategy for PMSM utilizing an extended state observer was proposed. This strategy incorporated unknown load disturbances into the system state to enhance observation accuracy. However, the observer involved numerous parameters that were challenging to tune. In [23, 24], a traditional sliding mode observer (SMDO) was used to observe load disturbances. This method enhances the system's immunity to interference. However, the coupling of torque error with speed causes the system to experience significant chattering, and the response time remains relatively long. To overcome these problems, this paper proposes a sliding mode disturbance observer with decoupling based on a new power exponential reaching law to observe load disturbances and with real-time feedback compensation based on the observed values.

In this paper, an improved model predictive torque control (IMPTC) strategy incorporating a decoupled sliding mode disturbance observer (DSMDO) is proposed. The cost function is first divided into two components that are sequentially evaluated, thereby achieving optimization without the need for weighting factors. A voltage vectors (VVs) modulation technique is subsequently employed to expand the VVs set, complemented by a low-complexity sector determination method that reduces the candidate VV from 32 to 7. Furthermore, the duration of the optimal VV is precisely optimized, which enhances flux control performance while reducing computational complexity. Finally, a novel sliding mode disturbance observer with decoupling capability is introduced, incorporating feedforward compensation into the speed control loop to improve disturbance rejection. Experimental results validate the effectiveness of the proposed strategy, showing significant reductions in torque and flux ripples, and enhanced robustness against load disturbances.

The subsequent sections of this paper are structured as follows. Section 2 formulates the mathematical model of the PMSM. Section 3 outlines the principles and implementation process of the conventional MPTC strategy. The design principles of the IMPTC method are discussed in Section 4. Section 5 details the experimental conditions and platform, followed by a validation analysis based on the experimental results. Finally, the conclusions drawn from both theoretical and experimental perspectives are presented in Section 6.

2. MATHEMATICAL MODELS

2.1. Model of PMSM

Neglecting the effect of the core saturation loss of the PMSM, the voltage equation of the PMSM under the d-q axis system can be represented as [25]:

$$\begin{cases} u_d = R_s i_d + \dfrac{d\psi_d}{dt} - \omega_e \psi_q \\ u_q = R_s i_q + \dfrac{d\psi_q}{dt} + \omega_e \psi_d \end{cases} \tag{1}$$

where u_d, u_q, i_d, i_q represent the d-q axis stator voltages and stator currents, respectively. The stator flux linkages are represented by ψ_d and ψ_q. R_s indicates stator resistance, and ω_e is the electrical angular velocity.

For surface-mounted permanent magnet synchronous motor (SPMSM), the inductances along the d-axis (L_d) and q-axis (L_q) are approximately equal under typical operating conditions. This assumption simplifies the control design and is valid for the motor considered in this study, where $L_d \approx L_q$.

The stator flux in d-q axis can be represented as:

$$\begin{cases} \psi_d = L_d i_d + \psi_f \\ \psi_q = L_q i_q \end{cases} \tag{2}$$

The electromagnetic torque is represented as:

$$T_e = \frac{3}{2} p_n \psi_f i_q \tag{3}$$

where T_e and p_n are the electromagnetic torque and the number of pole pairs, respectively. ψ_f is the permanent magnet flux linkage.

The mechanical motion equation of the motor is expressed as:

$$\frac{d\omega_e}{dt} = \frac{p_n}{J}\left(T_e - T_L - B\omega_m\right) \tag{4}$$

where J and B are the rotational inertia and system friction coefficient, respectively. T_L and ω_m represent load torque and mechanical speed, respectively.

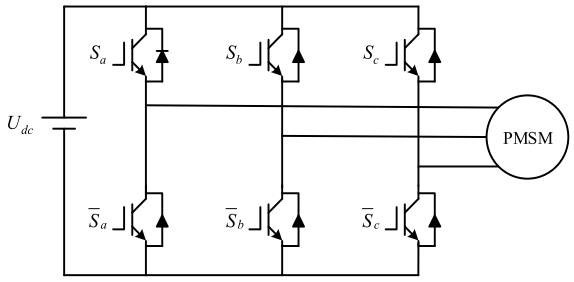

FIGURE 1. The circuit topology of the 2L-VSI.

2.2. Power Inverter

The inverter used in this paper is a two-level voltage source inverter (2L-VSI) [26]. The circuit topology of the 2L-VSI is shown in Fig. 1. Fig. 2 shows the voltage vectors generated by the 2L-VSI. The voltage equation is expressed as follows:

$$u_i = \frac{2}{3} U_{dc} \left(S_a + S_b e^{\frac{j2\pi}{3}} + S_c e^{\frac{j4\pi}{3}} \right) \tag{5}$$

where U_{dc} represents the DC-link voltage of the inverter, and (S_a, S_b, S_c) is the switch status of the inverter.

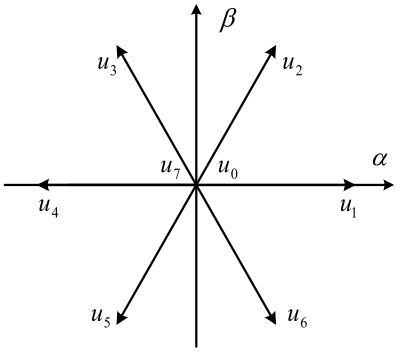

FIGURE 2. Vectors of the 2L-VSI.

3. CONVENTIONAL MPTC STRATEGY

To facilitate practical engineering applications, (1) and (2) are discretized by Euler method. The current at time step $k+1$ is represented as:

$$\begin{cases} i_d^{k+1} = \left(1 - \frac{T_s R_s}{L}\right) i_d^k + \omega_e T_s i_q^k + \frac{T_s}{L} u_d^k \\ i_q^{k+1} = \left(1 - \frac{T_s R_s}{L}\right) i_q^k + \omega_e T_s i_d^k + \frac{T_s}{L} u_q^k - \frac{\omega_e T_s}{L} \psi_f \end{cases} \tag{6}$$

where T_s is the system control period.

In real control processes, as the prediction calculations occupy most of the control cycle, delays are introduced into the system, preventing the motor speed from achieving optimal tracking performance. To compensate for these delays, the controlled variables at time step $k+2$ are iteratively predicted at the present moment.

The current at time step $k+2$ is represented as:

$$\begin{cases} i_d^{k+2} = \left(1 - \frac{T_s R_s}{L}\right) i_d^{k+1} + \omega_e T_s i_q^{k+1} + \frac{T_s}{L} u_d^{k+1} \\ i_q^{k+2} = \left(1 - \frac{T_s R_s}{L}\right) i_q^{k+1} + \omega_e T_s i_d^{k+1} + \frac{T_s}{L} u_q^{k+1} \\ \qquad - \frac{\omega_e T_s}{L} \psi_f \end{cases} \tag{7}$$

Substituting (7) into (2), the stator flux at time $k+2$ is represented as:

$$\begin{cases} \psi_d^{k+2} = \psi_f + L_d i_d^{k+2} \\ \psi_q^{k+2} = L_q i_q^{k+2} \end{cases} \tag{8}$$

From (8), the stator flux magnitude is represented as:

$$\left|\psi_s^{k+2}\right| = \sqrt{\left(\psi_d^{k+2}\right)^2 + \left(\psi_q^{k+2}\right)^2} \tag{9}$$

The electromagnetic torque at time step $k+2$ is expressed as:

$$T_e^{k+2} = \frac{3}{2} P_n \psi_f i_q^{k+2} \tag{10}$$

The reference stator flux amplitude is expressed as:

$$\left|\psi_s^{ref}\right| = \sqrt{\psi_f^2 + \left(\frac{2T_e^{ref} L}{3P_n \psi_f}\right)^2} \tag{11}$$

where T_e^{ref} is the reference torque, ψ_s^{ref} is the reference stator flux.

In the conventional MPTC strategy, the cost function is expressed as:

$$J = \left(T_e^{ref} - T_e^{k+2}\right)^2 + \lambda \left(\left|\psi_s^{ref}\right| - \left|\psi_s^{k+2}\right|\right)^2 \tag{12}$$

where λ is the weighting factor.

In the conventional MPTC, the reference torque value T_e^{ref} is obtained from the output of the speed loop proportional-integral (PI) controller. In practice, conventional MPTC control strategies traverse only seven voltage vectors (VVs) because zero vectors are usually unnecessary or redundant, while non-zero VVs are sufficient to achieve the desired output voltage and torque. Therefore, the use of seven VVs significantly reduces the amount of computation while ensuring the stability and performance of the system. The seven candidate VVs are used to calculate the predicted values of torque and flux through the prediction (7). Subsequently, the corresponding voltage vector is derived by minimizing the cost function J. Finally, the corresponding pulse signals are generated and sent to the inverter. Fig. 3 illustrates the control block diagram of the conventional MPTC.

4. IMPTC STRATEGY

4.1. Optimization of the Cost Function

In traditional methods, the adjustment of weighting factors often leads to an increase in computational complexity and a decrease in optimization accuracy. Particularly under varying load and operating conditions, frequent manual adjustments of the weighting factors can negatively affect the stability and response speed of the control. To overcome this issue, the step-by-step optimization method proposed in this paper first optimizes the torque cost function J_1, followed by the flux linkage cost function J_2, which avoids the uncertainty introduced by

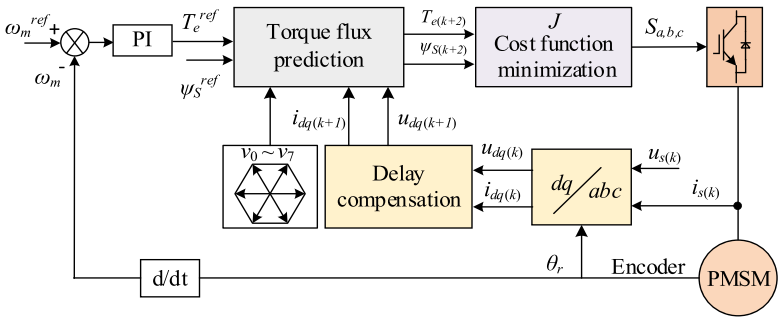

FIGURE 3. Control block diagram of the conventional MPTC.

the weighting factor adjustment and significantly reduces computational effort.

$$\begin{cases} J_1 = \left(T_e^{ref} - T_e(k+2)\right)^2 \\ J_2 = \left(\left|\psi_s^{ref}\right| - |\psi_s(k+2)|\right)^2 \end{cases} \tag{13}$$

Specifically, the optimization in Step 1 focuses on minimizing torque first, which quickly narrows down the candidate voltage vectors. This process reduces the number of voltage vectors considered, thus decreasing the computational burden. Then, Step 2 further optimizes the flux linkage cost function J_2, allowing for a precise selection of the final optimal voltage vector. The advantage of this sequential optimization approach is that it avoids the trial-and-error process and computational uncertainty associated with weighting factor adjustment in traditional methods, ensuring improved control accuracy and a more efficient control process.

By implementing this method, we not only reduce the computational effort but also enhance control accuracy and stability through a more systematic optimization process. Therefore, this step-by-step optimization method significantly reduces computational complexity while ensuring system performance.

Since torque control in MPTC has a higher priority than flux linkage control, reversing the two priorities would result in the motor's failing to achieve the desired control effect. Therefore, the proposed strategy evaluates J_1 first. First, all candidate voltage vectors are optimized in J_1. Two voltage vectors that minimize J_1 are identified and further evaluated in J_2 resulting in the optimal voltage vector.

4.2. Expansion of Voltage Vectors

The limitations of the traditional 2L-VSI topology, which can only generate eight basic voltage vectors (VVs), restrict the motor's dynamic performance and control precision. To overcome these limitations and improve system performance, multilevel topologies are often considered. Multilevel topologies can offer a greater number of VVs, enhancing the control accuracy and dynamic response of the motor. However, this increased complexity in both hardware and software also raises the overall system cost.

In this study, a formal 2L-VSI topology is employed, and a voltage vector modulation (VVM) method is integrated into the IMPTC method to enhance the number of VVs. This method generates new virtual VVs by linearly combining two adjacent basic VVs within each sector [27].

The α-β plane is divided into six sectors, and every sector is further subdivided into five equal parts, resulting in five smaller regions with an angular span of 12 degrees each. In each small area, the virtual VVs are expanded by combining the two active VVs at the boundary of the sector. This leads to virtual VVs that are uniformly distributed between the two active base VVs. Fig. 4 shows the virtual VVs and sector divisions. To facilitate differentiation, each of the original eight underlying VVs is assigned a new identifier, u_0, u_1, u_2, u_3, u_4, u_5, u_6, u_7 are represented by V_0, V_1, V_6, V_{11}, V_{16}, V_{21}, V_{26}, V_{31}, respectively. All VVs are assigned numbers in a counterclockwise direction, beginning with the basic voltage vector V_1 as the reference point.

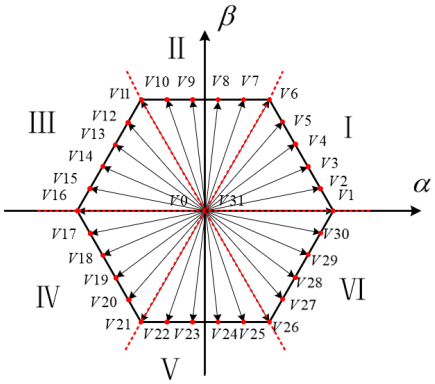

FIGURE 4. Virtual voltage vectors and sector divisions.

Compared to the original eight basic vectors, the application of numerous newly generated virtual VVs expands the candidate pool, thereby reducing the amplitude of torque ripple. However, the considerable increase in candidate vectors leads to a notable rise in computational burden.

To address the increased computational complexity, we adopt an optimization strategy that combines the sector selection algorithm with the limitation of hardware resources, reducing the dependence on computational resources. By predetermining the locations of candidate VVs and narrowing the range of candidate VVs, we improve the control accuracy and dynamic response without significantly increasing the hardware burden. This optimization strategy ensures that high

performance can still be achieved even with limited hardware resources.

4.3. Sector Determination

Considering the substantial increase in computational burden caused by enumerating all VVs in real systems, an effective approach is proposed.

Neglecting the effect of stator resistance R_s, the stator voltage vector (VV) is represented as [28]:

$$u_s = \frac{d\psi_s}{dt} \tag{14}$$

With the Euler discretization of (14) and introducing a one-tap delay, the error vector of stator flux is represented as:

$$\Delta\psi_s = u_{opt}T_s = \psi_s^{ref} - \psi_s(k+1) \tag{15}$$

where u_{opt} is the optimal VV, snf $\Delta\psi_s$ is the error vector of stator flux.

From (15), when u_{opt} acts on a whole T_s, it is equivalent to $\Delta\psi_s(\Delta\psi_s = u_{opt}T_s)$. As shown in Fig. 5, the direction of $\Delta\psi_s$ indirectly determines the direction of u_{opt} in a whole T_s.

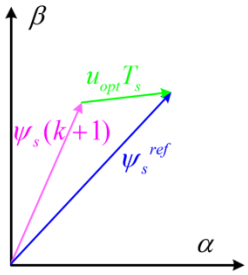

FIGURE 5. Relation between optimal VV and stator flux.

The position of u_{opt} can be identified by examining the signs of the real and imaginary components of $\Delta\psi_s$. This method does not require the calculation of the angle of u_{opt}, avoiding complex tangent calculations. After determining that u_{opt} lies within a specific sector on the α-β plane, all VVs within that sector can be considered as candidate solutions for selection. With this optimization strategy, the number of VVs traversed is significantly reduced, from the original 32 virtual VVs to just 7 vectors within the sector. Since the VVs within this sector are regarded as the most promising candidates, this effectively reduces the number of optimization iterations without sacrificing overall optimization accuracy. As a result, the number of iterations is reduced from 32 to 7, which not only significantly decreases the computational burden but also ensures high-quality system performance.

To facilitate the judgment of sectors, in this paper, the imaginary part of $\Delta\psi_s$ is denoted as $I_m(\Delta\psi_s)$. The real part of $\Delta\psi_s$ is denoted as $R_e(\Delta\psi_s)$. The ratio of the imaginary part to the real part of $\Delta\psi_s$ is denoted as m. $I_m(\Delta\psi_s)/R_e(\Delta\psi_s) = m$. The sector determination method is shown in Table 1.

4.4. Optimal Action Time Calculation

The final VV selected through the two cost functions may not fully achieve optimal tracking of torque and flux. To further minimize flux ripple, this paper proposes a method using a projection technique to ascertain the optimal time for the application of the optimal VV (u_{opt}). The error vector of stator flux ($\Delta\psi_s$) can be minimized to achieve this goal. In accordance with the relation between u_{opt} and $\Delta\psi_s$ in the sector judgment above, the effect of u_{opt} is basically the same as that of $\Delta\psi_s$ when acting throughout the control cycle T_s. Therefore, controlling the action time of u_{opt} enables the reduction of the flux ripple.

TABLE 1. Sector determination table.

m	$I_m(\Delta\psi_s)$	$R_e(\Delta\psi_s)$	sector
$(0, \sqrt{3}]$	> 0	> 0	I
$(-\infty, -\sqrt{3}) \cup (\sqrt{3}, +\infty)$	—	> 0	II
$[-\sqrt{3}, 0]$	> 0	< 0	III
$(\sqrt{3}, +\infty)$	> 0	< 0	IV
$(-\infty, -\sqrt{3}) \cup (\sqrt{3}, +\infty)$	< 0	—	V
$(-\sqrt{3}, 0)$	< 0	> 0	VI

As shown in Fig. 6, assume that $\Delta\psi_s$ is located in the first sector, and u_{opt} is replaced by V_1. When V_1 acts for the whole cycle T_s, it is recorded as the vector $T_s \cdot V_1$. At this point, it will generate a large next-moment error vector of stator flux $\Delta\psi_s(k+2)$. However, if V_1 acts on only a portion of T_s, $\Delta\psi_s(k+2)$ can be further reduced, thereby achieving better flux tracking performance. The optimal action time t_{opt} can be determined by calculating the ratio of the modulus of $\Delta\psi_s$ projected on V_1 to the modulus of the vector $T_s \cdot V_1$.

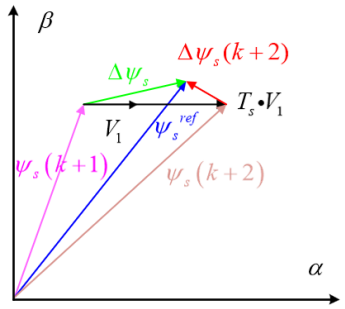

FIGURE 6. Effect of optimal VV action.

As shown in Fig. 7, after applying the projection method, the minimum distance between ψ_s^{ref} and vector $T_s \cdot V_1$ is the optimized $\Delta\psi_s(k+2)$, which is a vector perpendicular to $t_{opt} \cdot V_1$. The error of stator flux is then further minimized.

Therefore, the optimal action time is expressed as:

$$t_{opt} = \frac{\Delta\psi_s \cdot T_s u_{opt}}{T_s u_{opt} \cdot T_s u_{opt}} T_s \tag{16}$$

where "·" indicates the inner product of two vectors.

It is important to note that $\Delta\psi_s$ utilized in calculating the optimal action time in (16) is also employed in the sector determination. This approach avoids any additional computational load and effectively reduces the overall complexity.

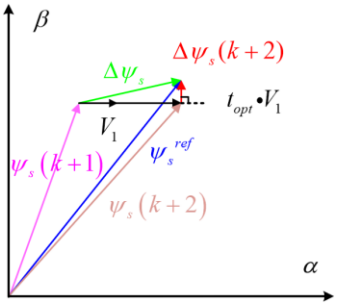

FIGURE 7. Effect of optimized optimal VV action.

In general, the optimal action time t_{opt} will be between 0 and T_s. However, when the modulus of the projection of $\Delta\psi_s$ on vector $T_s \cdot V_1$ is longer than the modulus of vector $T_s \cdot V_1$, t_{opt} is greater than T_s, which is unreasonable. To ensure that t_{opt} remains within the range of $0 \sim T_s$, any value outside this range must be adjusted accordingly. It is essential to adjust the optimal action time. The details and treatment are as follows:

$$\begin{cases} t_{best} = T_s & t_{opt} > T_s \\ t_{best} = t_{opt} & 0 \le t_{opt} \le T_s \end{cases} \tag{17}$$

where t_{best} is the optimized action time.

4.5. Design of the Decoupled Sliding Mode Disturbance Observer

In order to further enhance the anti-disturbance performance, a decoupled sliding mode disturbance observer (DSMDO) is designed. Considering the problem of significant jitter and long response times during the sliding mode observation, the conventional sliding mode disturbance observer (SMDO) is refined for better performance.

The schematic structure diagram of the DSMDO is shown in Fig. 8. Since the torque value is not easy to measure, i_q is used to calculate the torque value, which is used as an input to the observer along with the commanded mechanical speed. The observed load disturbance is used as the output.

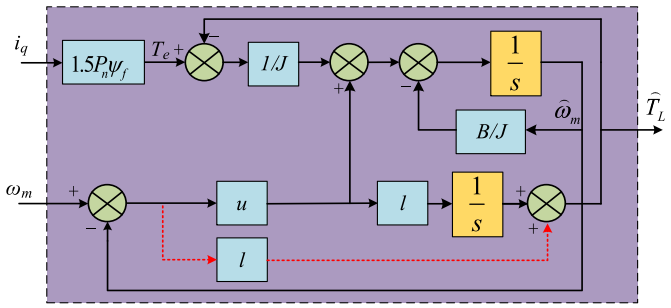

FIGURE 8. Block diagram of the DSMDO.

According to (4), the motor equation of motion can be rewritten as:

$$\begin{cases} \dot{\omega}_m = \frac{1}{J} T_e - \frac{B}{J} \omega_m - \frac{1}{J} T_L \\ \dot{T}_L = 0 \end{cases} \tag{18}$$

From (18), considering the mechanical speed ω_m and the load perturbation T_L as observation objects, the novel sliding mode observer equation can be obtained as:

$$\begin{cases} \dot{\widehat{\omega}}_m = \frac{1}{J} T_e - \frac{B}{J} \widehat{\omega}_m - \frac{1}{J} \widehat{T}_L + u(e_\omega) \\ \dot{\widehat{T}}_L = lu(e_\omega) + l\dot{e}_\omega \end{cases} \tag{19}$$

where $u(e_\omega)$ is the sliding mode control law corresponding to the speed observation error $e_\omega (e_\omega = \omega_m - \widehat{\omega}_m)$; $l (l < 0)$ is the observer gain; and $l\dot{e}_\omega$ is the speed error decoupling term in the load torque disturbance.

When the decoupling term $l\dot{e}_\omega$ is added to the observer, the error equation of the disturbance observer can be obtained from (18) and (19):

$$\begin{cases} \dot{e}_\omega = -\frac{1}{J} e_T - u(e_\omega) \\ \dot{e}_T = -lu(e_\omega) - l\dot{e}_\omega \end{cases} \tag{20}$$

where $e_T (e_T = T_L - \widehat{T}_L)$ is the load disturbance observation error.

Combining the two equations in (20) and eliminating the $u(e_\omega)$:

$$\dot{e}_T = \frac{l}{J} e_T \tag{21}$$

From (21), the load disturbance observation error e_T is expressed as:

$$e_T = Ce^{\frac{l}{J}t} \tag{22}$$

where C is a constant.

For the conventional SMDO, since the sliding mode observer equation $\widehat{T}_L = lu(e_\omega)$, the load disturbance observation error e_{T2} is expressed as:

$$e_{T2} = Ce^{\frac{l}{J}t} + l\left(\int e^{-\frac{l}{J}t} e_\omega dt\right) e^{\frac{l}{J}t} \tag{23}$$

From (23), it can be seen that when the system is far away from the sliding mode surface ($|s| > 1$), the speed coupling term $l(\int e^{-\frac{l}{J}t} e_\omega dt) e^{\frac{l}{J}t}$ will not be zero, which does not allow the load disturbance error to converge quickly, and a large jitter signal will be generated.

Comparing (22) and (23), by adding the decoupling term, the load disturbance observation error in the improved sliding mode disturbance observer does not contain the speed error coupling term. Therefore, by adding the decoupling term, the system jitter can be effectively reduced.

To further eliminate the steady-state error and improve the stability, the integral sliding mode surface is selected:

$$s = e_\omega + c \int_0^t e_\omega dt \tag{24}$$

where c is the integration coefficient of the integrating sliding mode surface.

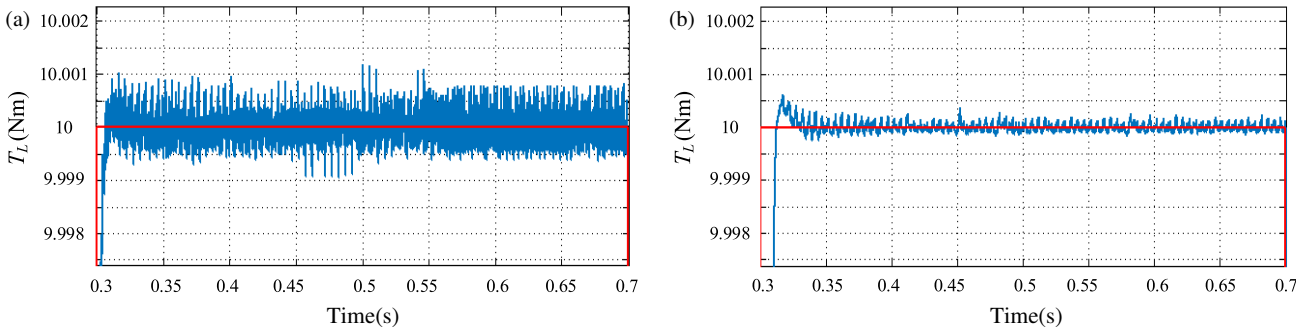

FIGURE 9. Observed load torque fluctuation diagram. (a) Conventional SMDO. (b) DSMDO.

Derived from (24):

$$\dot{s} = \dot{e}_\omega + ce_\omega \tag{25}$$

Combined with [23] and [24], a novel finite-time stabilized exponential power reaching law is proposed:

$$\dot{s} = -k_1 |s|^{|s|} \operatorname{sgn}(s) - k_2 |s|^a e^{-bt} \operatorname{sgn}(s) - k_3 s \tag{26}$$

where $k_1 > 0$, $k_2 > 0$, $k_3 > 0$, $0 < a < 1$, $b > 0$, e^{-bt} is an exponential function.

For (26), when the system state is far away from the sliding mode surface ($|s| > 1$), the term $-k_1|s|^{|s|}\operatorname{sgn}(s)$ plays a dominant role, and this part makes the system state variable converge to the sliding mode surface quickly. When the system state is close to the sliding mode surface ($|s| < 1$), the term $-k_2|s|^a e^{-bt}\operatorname{sgn}(s)$ plays a dominant role, and the exponential function e^{-bt} makes the system slow down the speed of reaching the sliding mode surface ($|s| = 0$), and the term $-k_3 s$ is used to realize the smooth transition of the sliding mode surface.

Combining (20), (25), and (26), the control law of the improved sliding mode disturbance observer is expressed as:

$$\begin{aligned} u(e_\omega) &= ce_\omega - \frac{1}{J} e_T + k_1 |s|^{|s|} \operatorname{sgn}(s) \\ &\quad + k_2 |s|^a e^{-bt} \operatorname{sgn}(s) + k_3 s \end{aligned} \tag{27}$$

Theorem: For the error (20), the control law of the improved sliding mode disturbance observer is designed as (27) by choosing the integral sliding mode surface (24) and the novel exponential power reaching law (26) such that e_ω and e_T converge in finite time.

Proof: The selected Lyapunov function V is as follows:

$$V = \frac{1}{2} s^2 \tag{28}$$

Taking the derivative of (28), the following expression is obtained:

$$\begin{aligned} \dot{V} &= s\dot{s} = s\Big(- k_1 |s|^{|s|} \operatorname{sgn}(s) \\ &\quad - k_2 |s|^a e^{-bt} \operatorname{sgn}(s) - k_3 s \Big) \le 0 \end{aligned} \tag{29}$$

From (29), it can be seen that $\dot{V} \le 0$. The state variables will reach the sliding mode surface in a limited time, and the designed observer can achieve the stabilization condition.

In order to demonstrate more convincingly how the DSMDO compares to a conventional SMDO, an observed load torque ($\widehat{T}_L$) tracking test was performed on both. In the test, a load of 10 N·m was applied to the system at 0.3 seconds and unloaded at 0.7 seconds. As can be seen in Fig. 9, the DSMDO is significantly better than the conventional SMDO in terms of amplitude control.

The value of the system disturbance observed by the improved sliding mode disturbance observer is used as a compensation signal and feed-forward compensated into the output torque of the speed ring. The expected value of the compensated torque is obtained:

$$T_e^{ref} = T_e^{PI} + \widehat{T}_L \tag{30}$$

The control block diagram of IMPTC is presented in Fig. 10. It includes four main components: Sector determination, model prediction, optimal action time calculation, and sliding mold disturbance observer.

5. EXPERIMENTAL VERIFICATION

To assess the feasibility and effectiveness of the proposed IMPTC, this paper utilizes RT-LAB to create a hardware-in-the-loop simulation experiment (HILS) platform, ensuring that the experimental results remain unaffected. The RT-LAB experimental platform is illustrated in Fig. 11, while the schematic diagrams are presented in Fig. 12. The digital signal processor (DSP) used is TMS320F2812, and other system components, such as the PMSM and inverter, are constructed using RT-LAB (OP5600). The parameters of the PMSM are detailed in Table 2. To ensure the fairness of the experiments, the same speed outer loop PI parameters are used for all strategies.

5.1. Steady-State Performance Analysis

This part compares the proposed IMPTC, conventional MPTC, and TSMPTC fro [19] by comparative testing of steady-state performance. The load torque is set to 10 N·m. The waveforms of the torque, stator flux, and A-phase current for the three strategies at 800 rpm, 1500 rpm, and 3000 rpm are shown in Figs. 13–15. The values of torque and stator flux ripple at

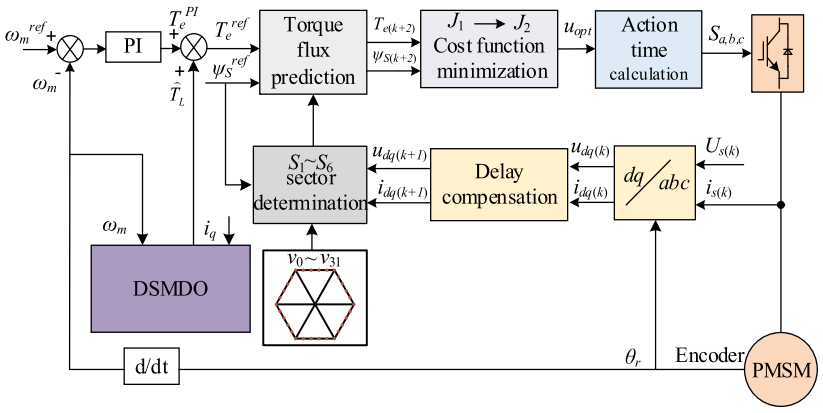

FIGURE 10. Control block diagram of the IMPTC.

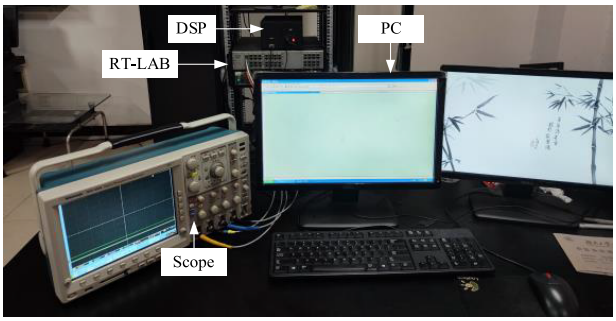

FIGURE 11. RT-LAB experimental platform.

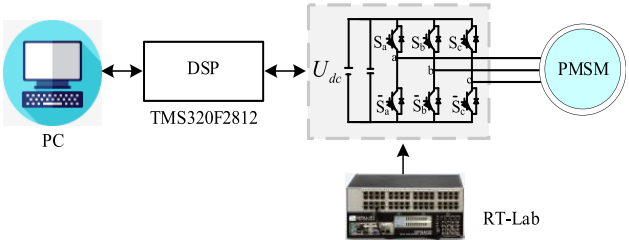

FIGURE 12. RT-LAB hardware-in-the-loop system.

TABLE 2. Motor parameters.

Parameter	Description	Value
U_{dc} (V)	DC voltage	300
P_n	Number of pole pairs	4
N (rpm)	Rated Speed	3000
ψ_f (Wb)	Permanent magnet flux	0.1
R_s (Ω)	Stator resistance	0.15
L (mH)	Stator inductance	0.001625
T_L (N·m)	Rated Torque	15
J (kg·m^2)	Rotational Inertia	0.000478

three speeds and the total harmonic distortion (THD) of the A-phase current are shown in Table 3.

From Figs. 13–15 and Table 3, it can be seen that the torque ripple and flux ripple of the proposed IMPTC are less than other strategies, both at high and low speeds. Additionally, the THD of the proposed IMPTC is lower than other strategies. Compared with conventional MPTC, the proposed IMPTC at 800 rpm reduces torque and flux ripples by 50.64% and 64.36%, respectively. The improvement in torque control performance of the proposed IMPTC is due to the expansion of the set of VVs along with removing the weighting factor, which results in a finer selection of the VV. In addition, owing to the further calculation of the action time of the optimal VV, the reference stator flux can be better tracked in the next control cycle.

5.2. Dynamic Performance Analysis

The proposed IMPTC is compared with conventional MPTC and TSMPTC in dynamic performance experiments. The working conditions are set as follows. The motor starts with no load, and the reference speed is 1000 rpm. The load torque T_L is loaded from 0 N·m to 10 N·m at 0.2 s. At 0.3 s, the speed is increased to 3000 rpm. At 0.6 s, the speed is decreased to 2000 rpm. At 0.7 s, the PMSM is unloaded; T_L is unloaded from 10 N·m to 0 N·m; and the experimental time is 1 s.

Figure 16 shows the speed, torque, stator flux, and the A-phase current of conventional MPTC, TSMPTC, and the proposed IMPTC, respectively.

From Fig. 16, it can be seen that the proposed IMPTC, conventional MPTC, and TSMPTC have similar speed response performance. This is because they have the same PI parameters for the speed outer loop. The speeds of the three control strategies fluctuate slightly during sudden load changes, but all of them are able to track quickly to a given speed. All three control strategies have a speed swing of 29.1 rpm and track to a given speed after 0.04 s.

5.3. Load Disturbance Performance Analysis

To verify the effectiveness of the decoupled sliding mode disturbance observer (DSMDO) designed in the proposed IMPTC strategy, simulated and experimental results are provided. The load disturbance resistance performances of IMPTC without SMDO IMPTC with traditional SMDO in [22] and IMPTC with

TABLE 3. Steady-state performance comparison.

Speed	Metrics	Conventional MPTC	TSMPTC	IMPTC
800 rpm	Torque ripple (N·m)	1.244	1.012	0.614
	Flux ripple (V·s)	0.00463	0.00493	0.00165
	THD (%)	5.69	5.51	2.93
1500 rpm	Torque ripple (N·m)	1.250	1.011	0.692
	Flux ripple (V·s)	0.00487	0.00470	0.00154
	THD (%)	5.74	5.56	2.94
3000 rpm	Torque ripple (N·m)	1.349	0.920	0.706
	Flux ripple (V·s)	0.00512	0.00440	0.00162
	THD (%)	577	5.21	2.97

TABLE 4. Load disturbance performance comparison.

Metrics	IMPTC without SMDO	IMPTC with traditional SMDO	IMPTC with DSMDO
Load speed ripple (rpm)	29.1	10.2	5.1
Unload speed ripple (rpm)	29.1	10.2	1.9
Load response time (s)	0.040	0.035	0.030

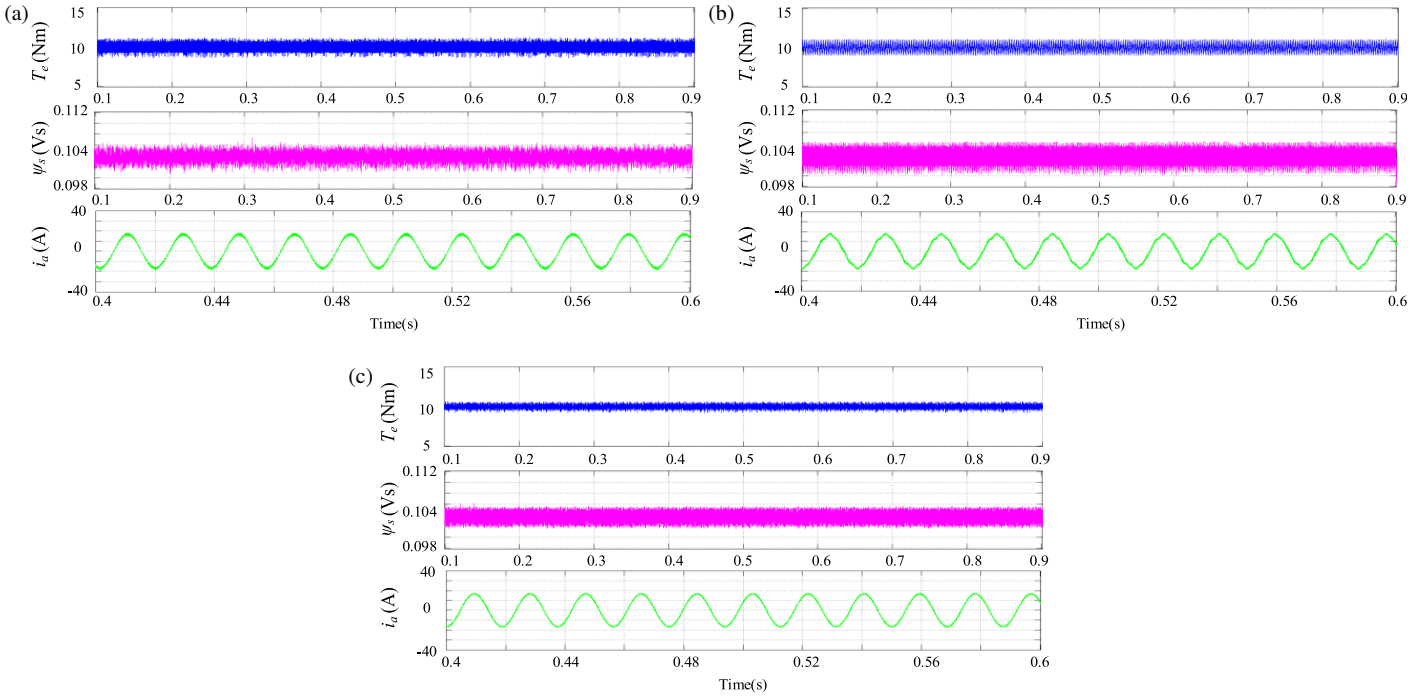

FIGURE 13. Steady-state experimental results at 800 rpm. (a) Conventional MPTC. (b) TSMPTC. (c) IMPTC.

DSMDO are compared in this part of the experiment. The motor starts with no load, and the reference speed is 3000 rpm. The load torque T_L is loaded from 0 N·m to 10 N·m at 0.2 s. At 0.7 s, the PMSM is unloaded; T_L is unloaded from 10 N·m to 0 N·m; and the experimental time is 1 s.

From Fig. 17 and Table 4, it can be seen that the DSMDO designed in this paper can effectively compensate the load disturbance, reduce the rotational speed pulsation, speed up the time of the system to recover the steady-state, and improve the system stability.

5.4. Code Execution Time and Number of Predictions Analysis

The traditional MPTC needs to traverse the cost function several times to find the optimal VV, and the algorithm execution

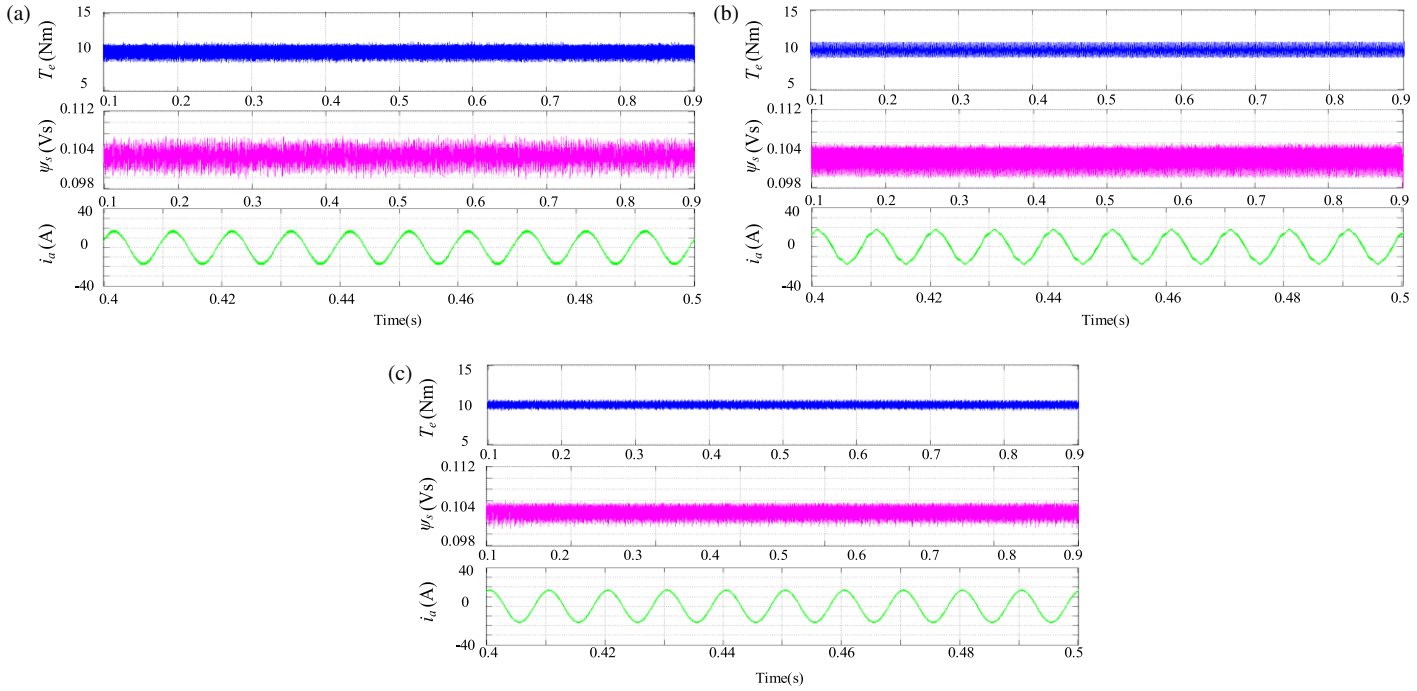

FIGURE 14. Steady-state experimental results at 1500 rpm. (a) Conventional MPTC. (b) TSMPTC. (c) IMPTC.

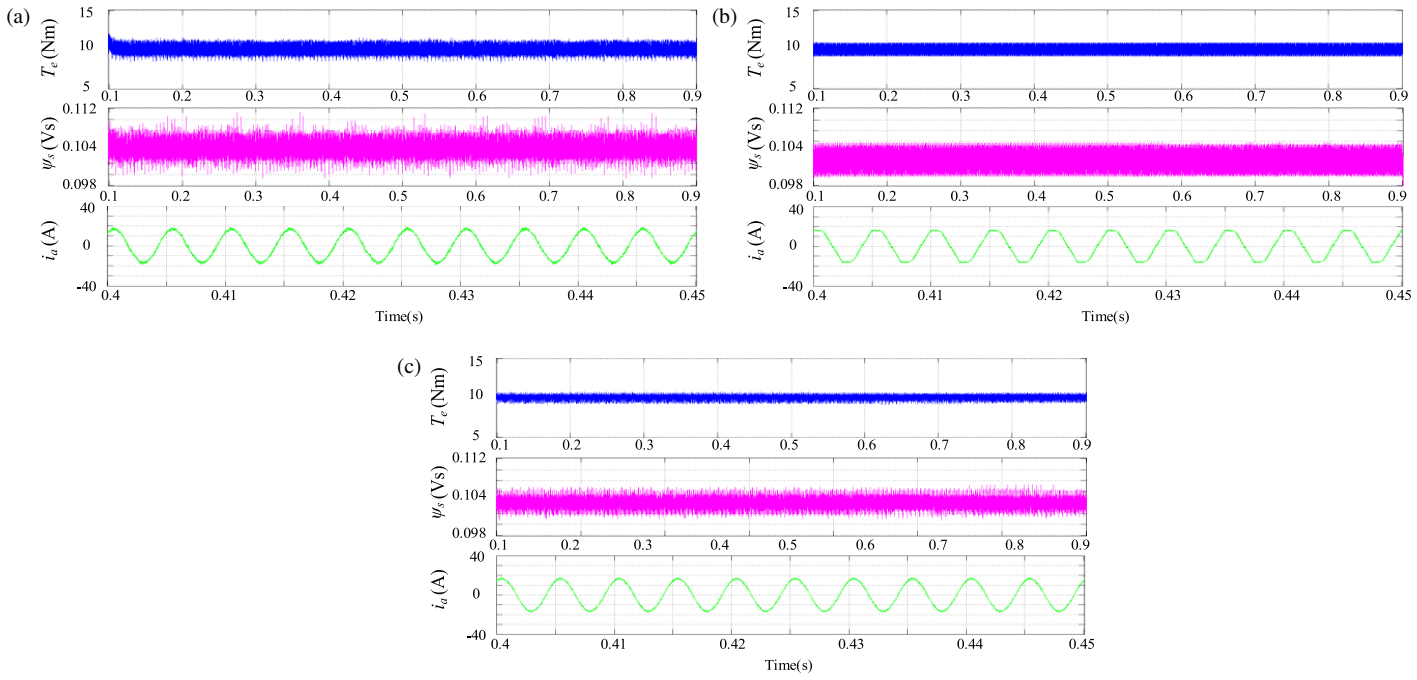

FIGURE 15. Steady-state experimental results at 3000 rpm. (a) Conventional MPTC. (b) TSMPTC. (c) IMPTC.

TABLE 5. Code execution time and number of predictions comparison.

Control strategy	Execution time	number of predictions
Conventional MPTC	42 μs	7
TSMPTC	45 μs	9
IMPTC	46 μs	9

time is long while the control effect is often poor. A comparison of the code execution time and number of predictions for the three strategies is shown in Table 5. Compared with the traditional MPTC, the code execution time of the proposed IMPTC is 46 μs, which is only increased by 9.5%. However, this is considered worthwhile compared to the optimization of the weighting factor and the improvement in torque control performance.

In conclusion, the experimental results demonstrate that the proposed IMPTC strategy not only effectively reduces the

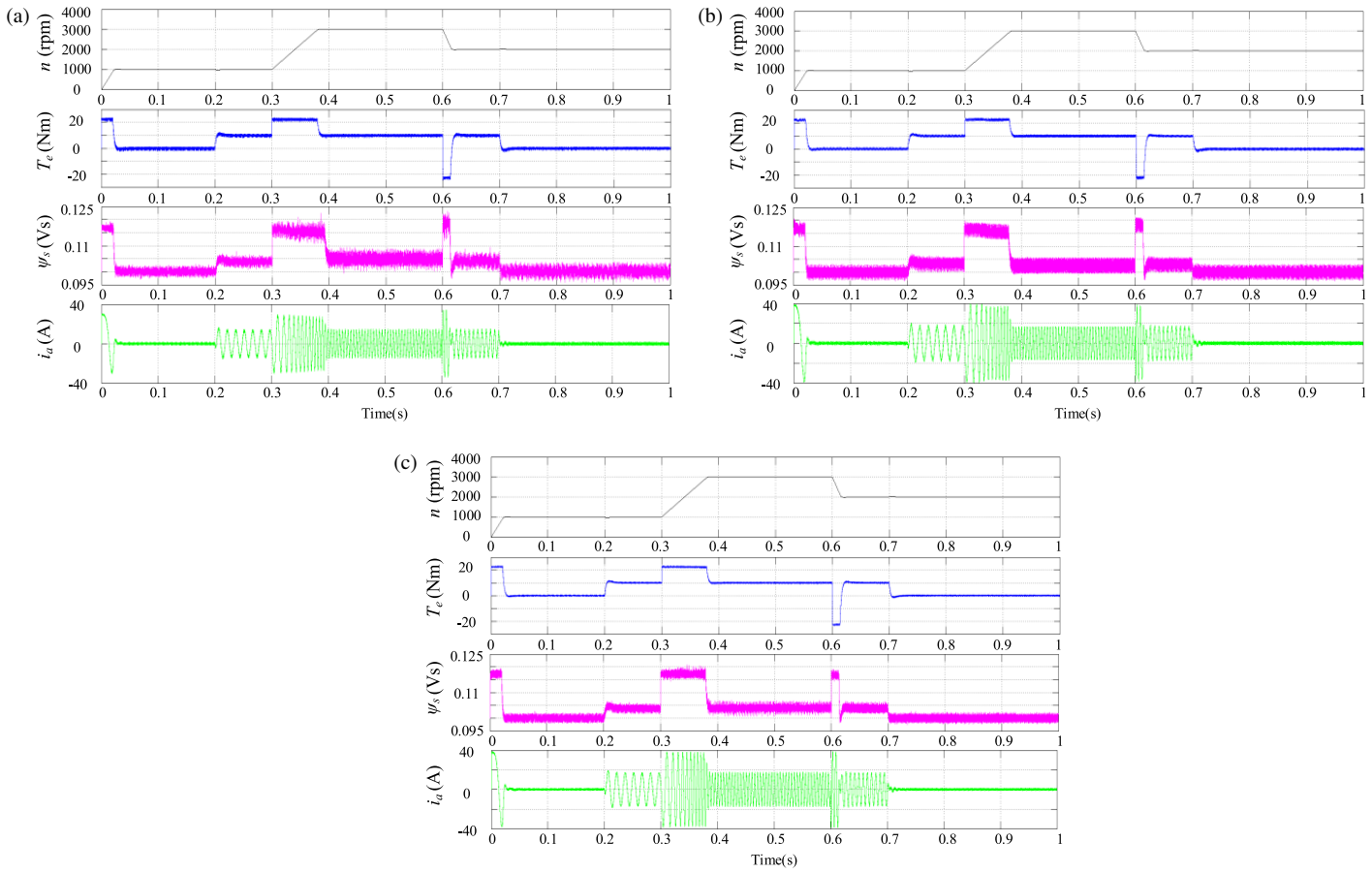

FIGURE 16. Dynamic experimental results. (a) Conventional MPTC. (b) TSMPTC. (c) IMPTC.

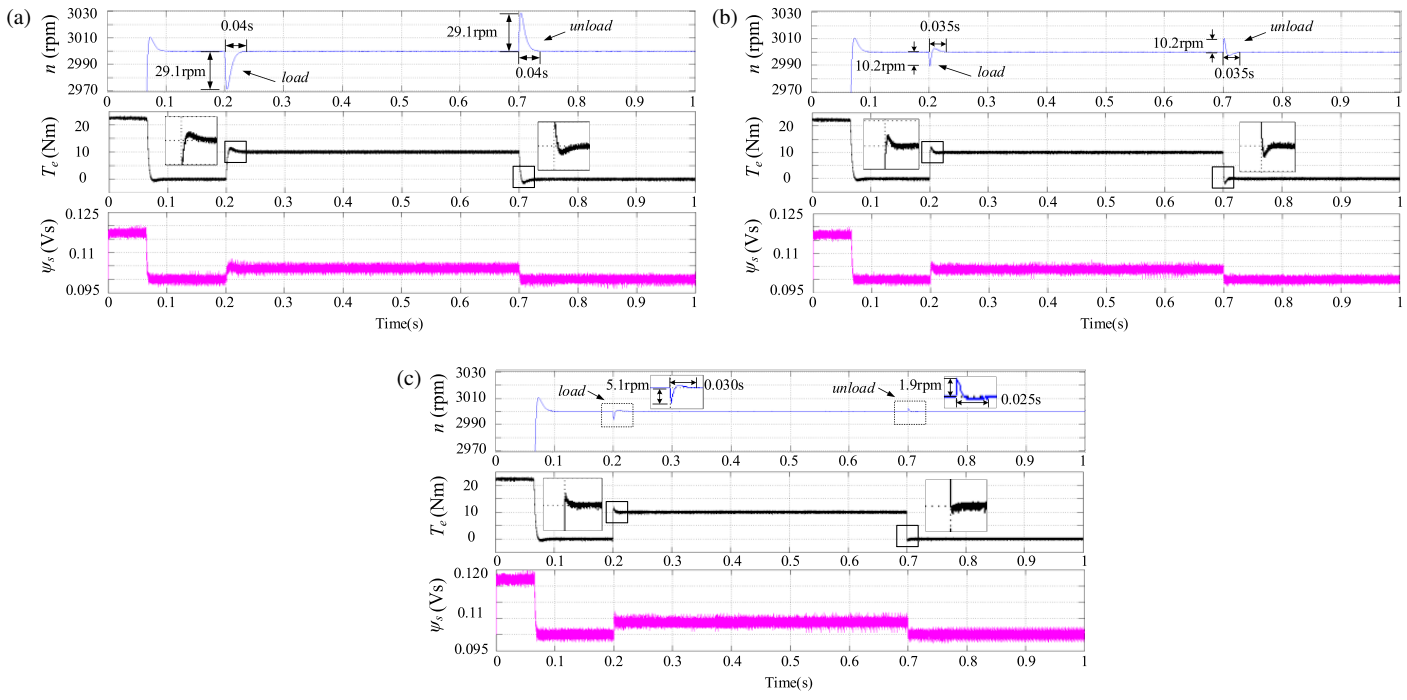

FIGURE 17. Load disturbance experimental results. (a) IMPTC without SMDO. (b) IMPTC with traditional SMDO. (c) IMPTC with DSMDO.

torque and stator flux ripples, thus improving the control performance, but also resists load disturbances and makes the motor run smoother, thus proving its potential for practical application in PMSM control.

6. CONCLUSION

In this paper, an improved model predictive torque control (IMPTC) strategy incorporating a decoupled sliding mode disturbance observer (DSMDO) is proposed to provide excellent performance for PMSM drivers. Through the theoretical elaboration and the analysis of experimental results, the conclusions are as follows:

1) The proposed IMPTC eliminates the weighting factor by dividing the cost function into two components and expands the VV set, which realizes a better torque control effect. Furthermore, the error vector of stator flux is used to determine the sector in which the optimal VV is located, and the computational burden of the system is further decreased.

2) Compared to the conventional MPTC, the proposed IMPTC further reduces flux ripple without additional computational burden by employing the error vector of stator flux to calculate the optimal action time.

3) The DSMDO designed is able to observe the unknown disturbance faster and more accurately. It performs feedforward compensation to improve the robustness of the system. When the load changes abruptly, the proposed IMPTC with DSMDO responds faster.

ACKNOWLEDGEMENT

This work was supported by the Natural Science Foundation of Hunan Province of China under Grant Number 2023JJ50191.

REFERENCES

[1] Wu, X., M. Yang, T. Wu, K. Lu, Y. Wang, X. Liu, S. Huang, and H. Cui, "Parameter-free predictive torque and flux control for PMSM based on incremental stator flux predictive model," *IEEE Transactions on Industrial Informatics*, Vol. 20, No. 2, 2715–2726, Feb. 2024.

[2] Xiao, Q., Z. Li, Y. Zhang, B. Luo, and T. Wang, "An improved low switching frequency three-vector model predictive torque control strategy for permanent magnet synchronous motors," *Progress In Electromagnetics Research C*, Vol. 126, 105–123, 2022.

[3] Petkar, S. G., K. Eshwar, and V. K. Thippiripati, "A modified model predictive current control of permanent magnet synchronous motor drive," *IEEE Transactions on Industrial Electronics*, Vol. 68, No. 2, 1025–1034, Feb. 2021.

[4] Jin, Z., X. Sun, G. Lei, Y. Guo, and J. Zhu, "Sliding mode direct torque control of SPMSMs based on a hybrid wolf optimization algorithm," *IEEE Transactions on Industrial Electronics*, Vol. 69, No. 5, 4534–4544, May 2022.

[5] Gao, J., C. Gong, W. Li, and J. Liu, "Novel compensation strategy for calculation delay of finite control set model predictive current control in PMSM," *IEEE Transactions on Industrial Electronics*, Vol. 67, No. 7, 5816–5819, Jul. 2020.

[6] An, X., G. Liu, Q. Chen, W. Zhao, and X. Song, "Adjustable model predictive control for IPMSM drives based on online stator inductance identification," *IEEE Transactions on Industrial Electronics*, Vol. 69, No. 4, 3368–3381, Apr. 2022.

[7] Zhang, Y. and H. Yang, "Model-predictive flux control of induction motor drives with switching instant optimization," *IEEE Transactions on Energy Conversion*, Vol. 30, No. 3, 1113–1122, Sep. 2015.

[8] Wang, F., J. Li, Z. Li, D. Ke, J. Du, C. Garcia, and J. Rodriguez, "Design of model predictive control weighting factors for PMSM using Gaussian distribution-based particle swarm optimization," *IEEE Transactions on Industrial Electronics*, Vol. 69, No. 11, 10 935–10 946, Nov. 2022.

[9] Davari, S. A., D. A. Khaburi, and R. Kennel, "An improved FCS-MPC algorithm for an induction motor with an imposed optimized weighting factor," *IEEE Transactions on Power Electronics*, Vol. 27, No. 3, 1540–1551, Mar. 2012.

[10] Yao, C., Z. Sun, S. Xu, H. Zhang, G. Ren, and G. Ma, "ANN optimization of weighting factors using genetic algorithm for model predictive control of PMSM drives," *IEEE Transactions on Industry Applications*, Vol. 58, No. 6, 7346–7362, Nov.–Dec. 2022.

[11] Hassan, M., X. Ge, A. T. Woldegiorgis, M. S. Mastoi, M. B. Shahid, R. Atif, M. S. Shaikh, and S. Kumar, "A look-up table-based model predictive torque control of IPMSM drives with duty cycle optimization," *ISA Transactions*, Vol. 138, No. 4, 670–686, Jul. 2023.

[12] Liu, R., H. Li, Y. Zhou, L. Yang, and J. Huang, "Equivalent weighting factor-based model predictive torque control of SMPMSM," *IEEE Journal of Emerging and Selected Topics in Power Electronics*, Vol. 11, No. 5, 4808–4817, Oct. 2023.

[13] Gong, C., Y. Hu, M. Ma, J. Gao, and K. Shen, "Novel analytical weighting factor tuning strategy based on state normalization and variable sensitivity balance for PMSM FCS-MPTC," *IEEE/ASME Transactions on Mechatronics*, Vol. 25, No. 3, 1690–1694, Jun. 2020.

[14] Wang, Y., S. Huang, X. Huang, W. Liao, J. Zhang, and B. Ma, "An angle-based virtual vector model predictive current control for IPMSM considering overmodulation," *IEEE Transactions on Transportation Electrification*, Vol. 10, No. 1, 353–363, Mar. 2024.

[15] Zhang, X. and Y. He, "Direct voltage-selection based model predictive direct speed control for PMSM drives without weighting factor," *IEEE Transactions on Power Electronics*, Vol. 34, No. 8, 7838–7851, Aug. 2019.

[16] Zhang, Y. and H. Yang, "Two-vector-based model predictive torque control without weighting factors for induction motor drives," *IEEE Transactions on Power Electronics*, Vol. 31, No. 2, 1381–1390, Feb. 2016.

[17] Lin, X., W. Huang, W. Jiang, Y. Zhao, and S. Zhu, "Predictive torque control for PMSM based on weighting factor elimination and fast voltage vector selection," *IEEE Journal of Emerging and Selected Topics in Power Electronics*, Vol. 8, No. 4, 3736–3750, Dec. 2020.

[18] Yang, M., X. Wu, S. Huang, W. Liao, T. Wu, Y. Wang, and S. Huang, "Enhanced model-free predictive speed control without weighting factors for PMSM based on newly designed cost function," *IEEE Transactions on Transportation Electrification*, Vol. 10, No. 3, 5703–5714, Sep. 2024.

[19] Norambuena, M., J. Rodriguez, Z. Zhang, F. Wang, C. Garcia, and R. Kennel, "A very simple strategy for high-quality performance of AC machines using model predictive control," *IEEE Transactions on Power Electronics*, Vol. 34, No. 1, 794–800, Jan. 2019.

[20] Zhang, Y., B. Zhang, H. Yang, M. Norambuena, and J. Rodriguez, "Generalized sequential model predictive control of

IM drives with field-weakening ability," *IEEE Transactions on Power Electronics*, Vol. 34, No. 9, 8944–8955, Sep. 2019.

[21] Zhang, K., M. Fan, Y. Yang, R. Chen, Z. Zhu, C. Garcia, and J. Rodriguez, "Tolerant sequential model predictive direct torque control of permanent magnet synchronous machine drives," *IEEE Transactions on Transportation Electrification*, Vol. 6, No. 3, 1167–1176, Sep. 2020.

[22] Wang, Y., Y. Feng, X. Zhang, J. Liang, and X. Cheng, "New reaching law control for permanent magnet synchronous motor with extended disturbance observer," *IEEE Access*, Vol. 7, 186 296–186 307, 2019.

[23] Wang, Q., H. Yu, M. Wang, and X. Qi, "An improved sliding mode control using disturbance torque observer for permanent magnet synchronous motor," *IEEE Access*, Vol. 7, 36 691–36 701, 2019.

[24] Woldegiorgis, A. T., X. Ge, H. Wang, and M. Hassan, "A new frequency adaptive second-order disturbance observer for sensorless vector control of interior permanent magnet synchronous motor," *IEEE Transactions on Industrial Electronics*, Vol. 68, No. 12, 11 847–11 857, Dec. 2021.

[25] Petkar, S. G. and V. K. Thippiripati, "Effective multivector-operated predictive current control of PMSM drive with reduced torque and flux ripple," *IEEE Transactions on Transportation Electrification*, Vol. 9, No. 2, 2217–2227, Jun. 2023.

[26] Amiri, M., J. Milimonfared, and D. A. Khaburi, "Predictive torque control implementation for induction motors based on discrete space vector modulation," *IEEE Transactions on Industrial Electronics*, Vol. 65, No. 9, 6881–6889, Sep. 2018.

[27] Wang, Y., X. Wang, W. Xie, F. Wang, M. Dou, R. M. Kennel, R. D. Lorenz, and D. Gerling, "Deadbeat model-predictive torque control with discrete space-vector modulation for PMSM drives," *IEEE Transactions on Industrial Electronics*, Vol. 64, No. 5, 3537–3547, May 2017.

[28] Li, X., Z. Xue, X. Yan, L. Zhang, W. Ma, and W. Hua, "Low-complexity multivector-based model predictive torque control for PMSM with voltage preselection," *IEEE Transactions on Power Electronics*, Vol. 36, No. 10, 11 726–11 738, Oct. 2021.